Supplementary Materials

Solar-driven all-solid-state lithium-air batteries operating at extreme low-temperatures

Hucheng Song[1], Sheng Wang[1], Xiaoying Song[1], Jue Wang[1], Kezhu Jiang[1], Shihua Huang[2], Min Han[1], Jun Xu[1]*, Ping He[1]*, Kunji Chen, Haoshen Zhou[13]*

[1] National Lab of Solid State Microstructures, Center of Energy Storage Materials & Technology College of Engineering and Applied Sciences, *National Laboratory of Solid State Microstructures/Collaborative Innovation Center of Advanced Microstructures and School of Electronics Science and Engineering, Nanjing University, Nanjing 210093, China*

[2]Physics Department, Zhejiang Normal University, Jinhua 321004, China

[3]Energy Technology Research Institute National Institute of Advanced Industrial Science and Technology (AIST) Umezono 1-1-1, Tsukuba 3058568, Japan

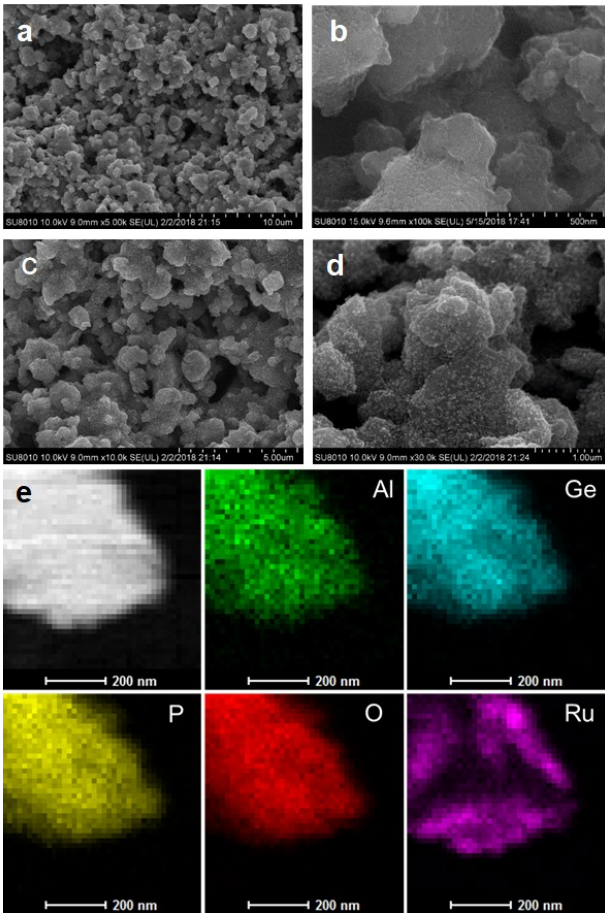

Fig. S1 SEM images of cathodes coated on LAGP electrolyte. (a, b) Traditional cathode consisting RuO_2 catalyst, electron-conducting CNT, ion-conducting LAGP and corresponding enlarge image. (c, d)

Plasmonic cathode prepared by assembling single-layer Ru nanostructures on traditional air cathode and corresponding enlarge image of plasmonic cathode. (e) STEM image of a single LAGP particle peeled from air cathode and (d) corresponding element EDX mappings of Al, Ge, P, O and Ru.

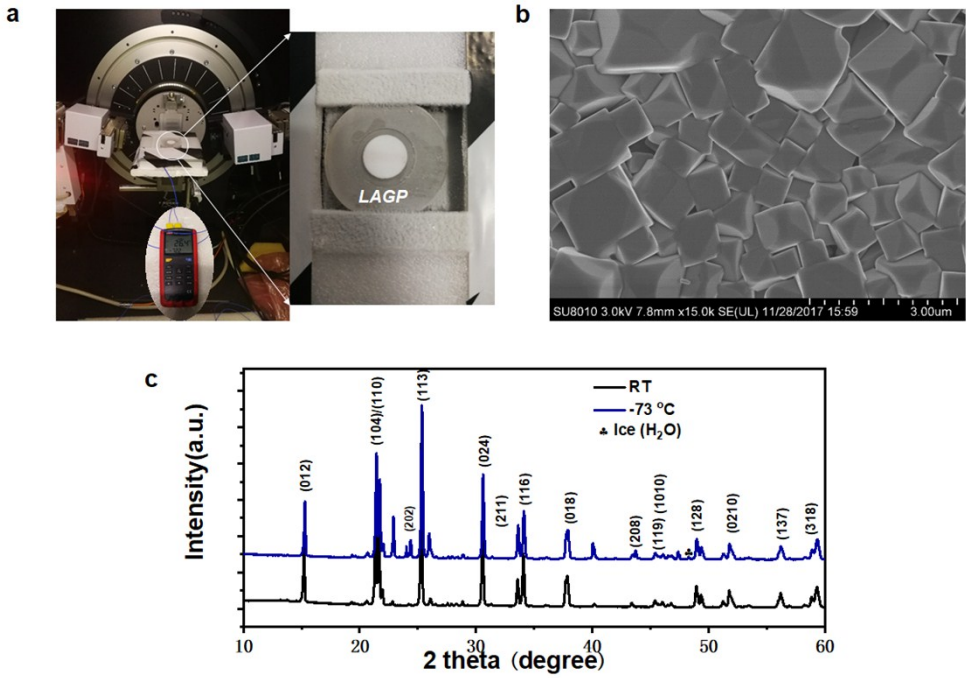

Fig. S2. Low-temperature XRD test system of prepared solid-state electrolyte (LAGP) that includes a LAGP electrolyte, a low-temperature environmental provided by dry ice and a temperature detector. The temperature is maintained at about -73 ^{o}C during the whole testing process. The room temperature (RT) is about 26 ^{o}C. (b) SEM image of LAGP electrolyte that consists of LAGP gains with a size distribution from ~500 nm to ~2.5 um. (c) X-ray diffraction patterns of the LAGP electrolyte over a wide temperature spectrum from -73 ^{o}C to 150 ^{o}C where the low-temperature test environmental is maintained by the dry ice.

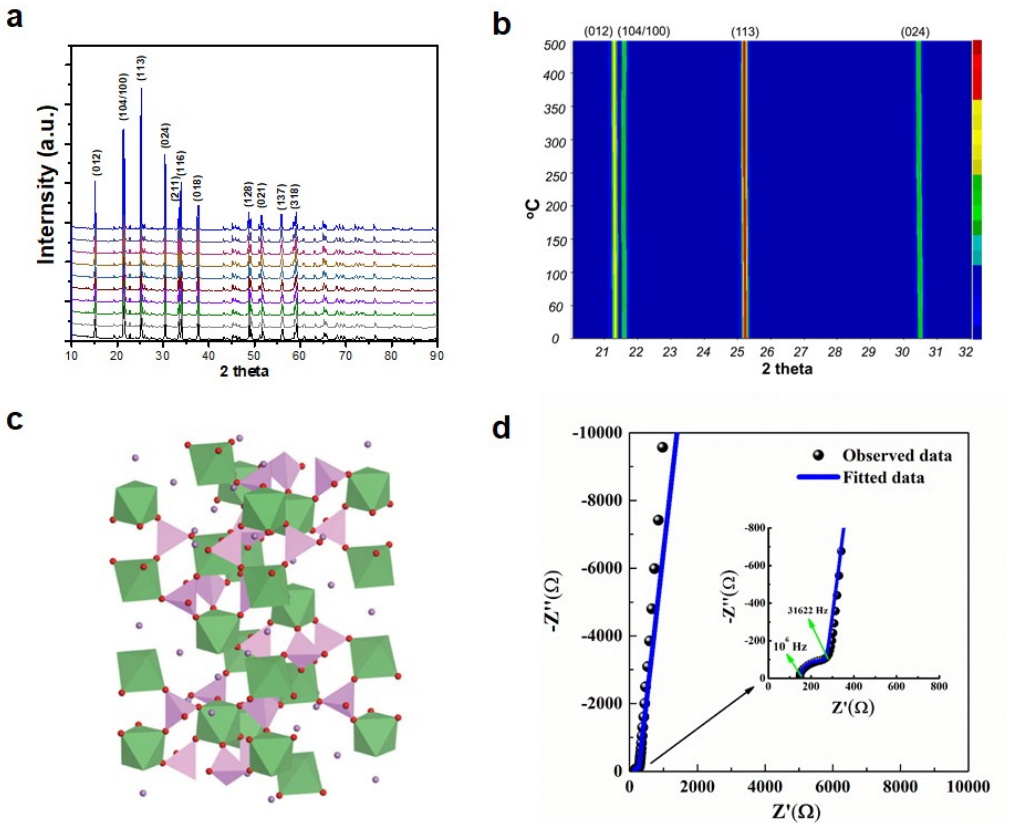

Fig. S3 (a, b) insitu-XRD analysis of prepared LAGP electrolyte under various temperatures. (c) Crystal structure of NASICON-type LAGP. (d) The electrochemical impedance spectroscopy plots of the LAGP electrolyte employing Au/LAGP/Au symmetric battery.

The stability of the electrolyte is crucial for exploiting high-density ASS lithium-ion batteries operating at extra-low/high temperatures. To study the structure stability of LAGP electrolytes over a wide temperature range, we conducted in-situ variable temperature XRD analysis on LAGP electrolyte where the strongest diffraction peaks located at 25.4°, 21.4° and 30.6°and 15.2°correspond to the crystalline planes of LAGP (113), (104)/(110), (024) and (012), respectively. Notably, the diffraction peak intensity and position have not changed as the temperature increases from -73 ^{o}C to 500 ^{o}C (Fig. S2b). These results indicate a robust structure of the LAGP electrolyte even at extreme low-/high-temperatures that demonstrates a rhombohedral structure with space group R3c, and an open three-dimensional framework sharing all corners of GeO_6 octahedra with PO_4 tetrahedra (Fig. S2c). Further, the electrochemical impedance spectrum of the LAGP electrolyte at room temperature was studied by Au/LAGP/Au symmetric battery. The perturbation voltage is 5 mV in the frequency range of 1 MHz to 0.1 Hz.

Two fitting resistances consisting of the bulk resistance (R1) and the grain boundary resistance (R2) were obtained. Among them, R_1 and R_2 are 251.8 Ω and 72.3 Ω, respectively. The thickness of (L) and the diameter (D) of the LAGP electrolyte are 0.1 cm and 1.7 cm, respectively. Therefore, the total conductivity of the LAGP electrolyte is about 3.9×10^{-4} S cm^{-1} that can be calculated by the following formula (1).

$$\sigma = \frac{L}{S \times R} \quad (1)$$

In this formula, S is the surface area of the LAGP electrolyte and R is the sum of R_1 and R_2

According to previous reported method, a traditional air cathode was prepared on the LAGP electrolyte by coating milled mixture of electron-conducting CNT, ion-conducting LAGP particles and RuO_2 catalysts that shows a porous structure (Fig. S3a) and a relatively smooth surface in enlarged illustration (Fig. S3 b). We cannot obviously observe the RuO_2 catalysts on the surface of traditional cathode. After a gas phase cluster beam deposition process, close-packed single-layer ruthenium nanostructures (size distribution is around 5 nm to 20 nm, as shown in Fig. S5a) were successfully assembled on traditional cathode, thus producing a plasmonic cathode as shown in Fig. S3d.

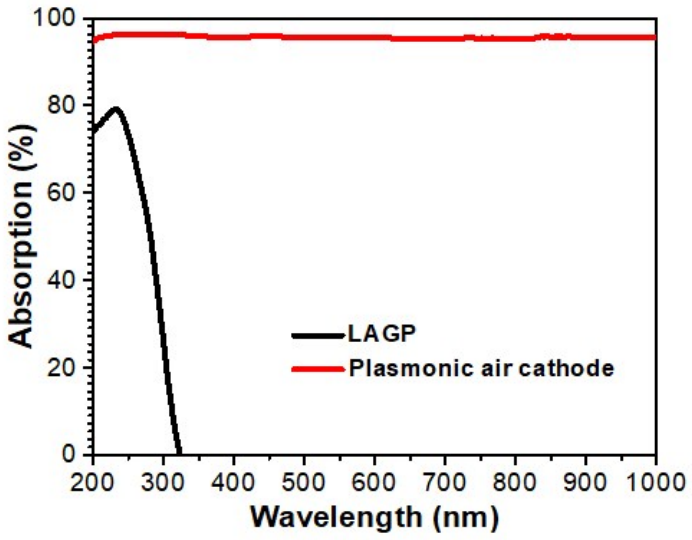

Fig. S4 Absorption spectrum of LAGP electrolyte and plasmonic cathode.

Optical reflectance and transmittance spectrum of LAGP electrolyte and plasmonic cathode coated on the SSE were characterized by the Shimadzu UV3600 spectrophotometer. The absorption efficiency is calculated by the formula: $A = 1 - R - T$ where R is the reflection efficiency, T is the transmission efficiency and A is the absorption efficiency. As shown in Fig. 2, LAGP solid-state electrolyte demonstrates an extra-high reflectance and more than 12% transmission in the visible and near infrared regions. After coating plasmonic cathode, the light reflection and transmission efficiencies are reduced to ~4.0% and <0.9%, respectively. Thus, an extra-high light absorption efficiency of more than 95% has been obtained at 200 nm to 2500 nm that indicate an efficient and broadband solar adsorption of plasmonic cathode from UV, visible to near infrared light.

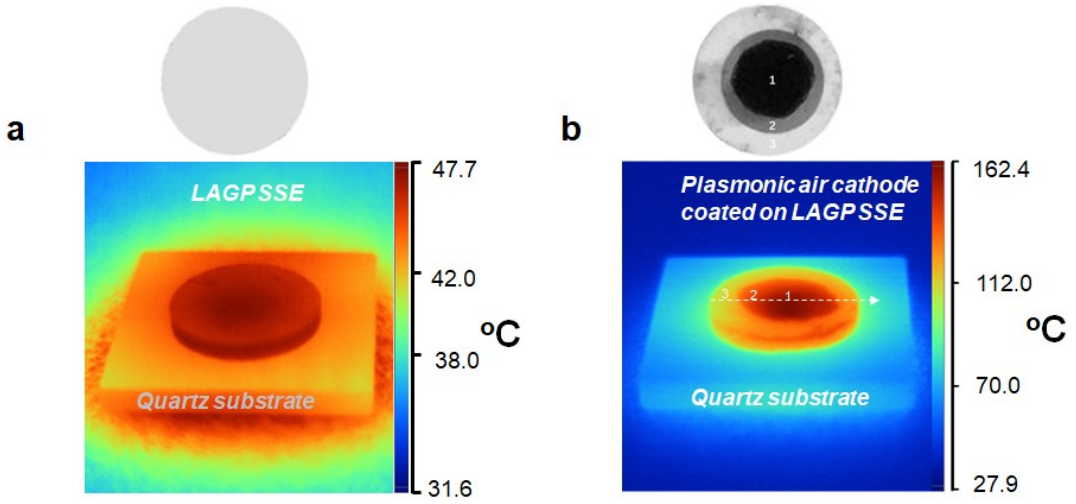

Fig. S5. Light-induced thermal heating of plasmonic air cathode. (a) IR image of the LAGP SSE (with ~1 um thick and ~1.6 cm diameter) under light irradiation (Xe-lamp, ~6.9 kW m^{-2}, 11 A) where a quartz is employed as the substrate. (b) IR image of the plasmonic air cathode coated on SSE under Xe-lamp irradiation, which shows three typical areas consisting of LAGP SSE (areal 3), Ru nanostructures (areal 2) and plasmonic air cathode (areal 1).

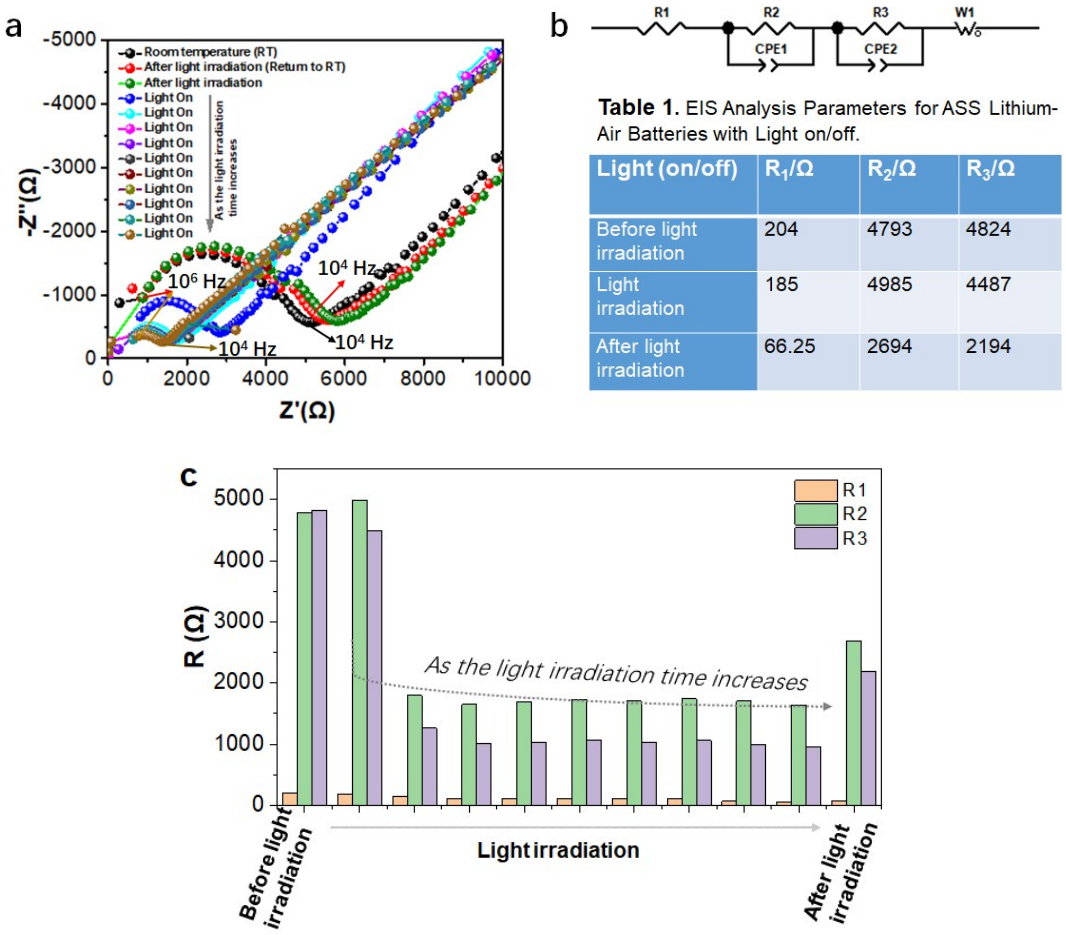

Table 1. EIS Analysis Parameters for ASS Lithium-Air Batteries with Light on/off.

Light (on/off)	R_1/Ω	R_2/Ω	R_3/Ω
Before light irradiation	204	4793	4824
Light irradiation	185	4985	4487
After light irradiation	66.25	2694	2194

Fig. S6. (a) Nyquist plots of ASS lithium-air battery at room temperature under Xe-lamp light irradiation on and off. (b, c) Equivalent circuit used for fitting and corresponding grain impedance (R1), grain boundary (R2) and interface charge-transport impedance (R3) under light irradiation on and off.

Fig. S6 shows the electrochemical impedance spectrum of the ASS lithium-air battery operating at room temperature with/without light irradiation that were analyzed by equivalent circuits with resistive (Ri)/capacitive (Ci) combination. The EIS fitting results of the equivalent circuit are listed in Table 1. Among them, R_1 is the grain impedance of electrolyte that can be defined by the intercept of the first semicircle and the horizontal axis. R_2 is the grain boundary resistance of electrolyte/electrodes that can be defined by the semicircle at high frequency region. R_3 is the interface charge-transfer impedance that can be defined by the semicircle at low frequency region. CPE_1 and CEP_2 are their associated capacitances. Wo is the Warburg di□usion contribution. As shown in Table 1, the grain impedance (R1), grain boundary impedance (R2) and

interface impedance (R3) of the ASS lithium-air battery at room temperature are 204 Ω cm^2, 4793 Ω cm^2 and 4824 Ω cm^2, respectively. Under light irradiation, all the resistances of the battery drastically reduced and finally maintained at a stable and smaller value where R_1 is 185 Ω cm^2, R_2 is 4985 Ω cm^2 and R_3 is 4487 Ω cm^2. It is indicated that light-induced thermal heating of the ASS lithium-air not only decrease the grain impedance and grain boundary resistances associated with electrolyte, but also remarkably decrease the interface charge-transport resistance of electrolyte/electrodes. Notably, the impedance spectrum of the battery returns to the state of room temperature after light irradiation, further indicating a robust and revertible photothermal operation.

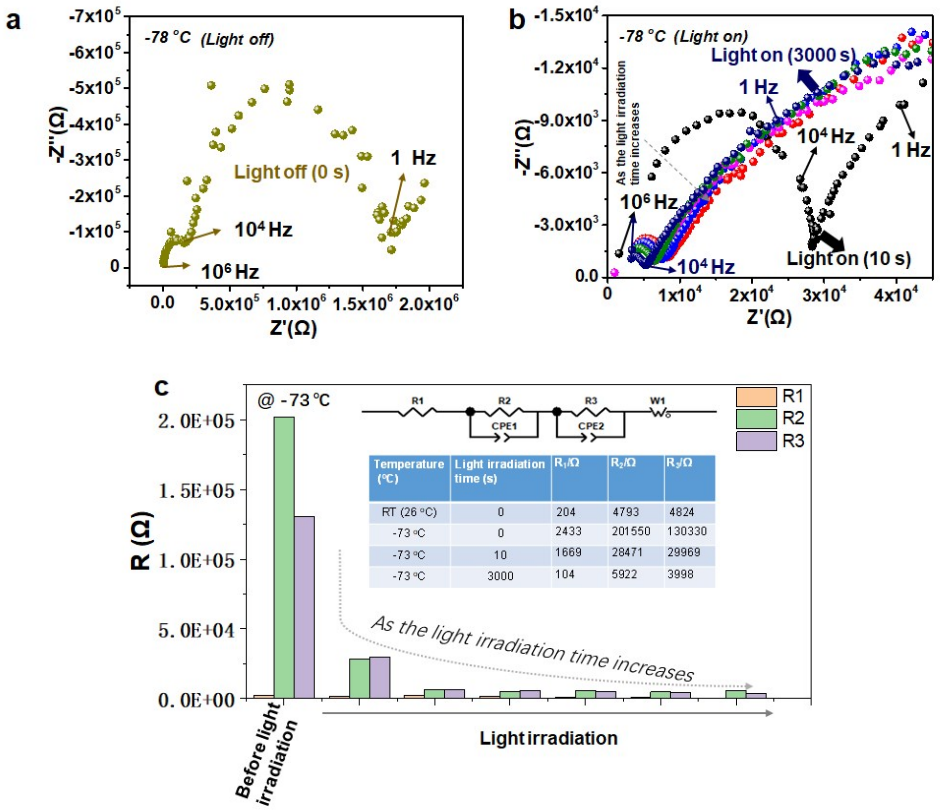

Fig. S7. Nyquist plots of all-soli-state Li-air battery operating at -73 °C. (a) Without light irradiation. (b) Under Xe-lamp light irradiation. (c) Equivalent circuit used for fitting and corresponding grain impedance (R1), grain boundary (R2) and interface charge-transport impedance (R3) with the increase of the light irradiation time.

The impedance spectra of the battery operating at -73 ^{o}C with/without light irradiation were further analyzed using equivalent circuits with resistive (Ri)/capacitive (Ci) combination. The EIS fitting results of the equivalent circuit are listed in Table 2 of Fig. S7c. Among them, R_1 represents the grain impedance of electrolyte. R_2 represents the grain boundary resistance of electrolyte and the electrodes. R_3 represents the interface charge-transfer impedance associated with electrolyte/electrodes. CPE_1 and CEP_2 are their corresponding capacitances as show in Fig. S7c. Wo is the Warburg di□usion contribution. When the ASS lithium-are battery is placed in a low temperature environment of -73 ^{o}C, the resistance associated with electrolyte/electrodes is ~10^5 Ω cm^2 Ω, especially grain boundary impedance and interface charge-transfer impedance (R_2: 2.0×10^5 Ω cm^2, R_3: 1.3×10^5 Ω cm^2), which is two orders of magnitude higher than that of the ASS lithium battery at room temperature (~10^3 Ω cm^2 Ω) as show in Table 2. Such extra-large impedance blocks the transmission of lithium-ions, thus making the ASS batteries lost all the capacity (without any discharge/charge behavior) during discharge/charge process. It is the main reason that the ASS batteries cannot operate at low temperatures. Surprisingly, under light irradiation, both grain boundary impedance and interface impedance associated with electrolyte/electrodes rapidly reduced to ~10^4 Ω cm^2 (R_2: 2.8×10^4 Ω cm^2 , R_3: 3.0×10^4 Ω cm^2) within 10 s and finally reached a steady state value of ~10^3 Ω cm^2 (R_2: 5.9×10^3 Ω cm^3 , R_3: 3.9×10^3 Ω cm^2) that is ~3% of the battery at -73 ^{o}C without light irradiation. The grain impedance (R_1) also reduced from ~2.4×10^3 Ω cm^2 to ~1.0×10^2 Ω cm^2 under light irradiation. Such resistances can be compared with the impedance of ASS lithium-air batteries at room temperature (R_1: ~2.0×10^2 Ω cm^2), R_2: ~4.7×10^3 Ω cm^2, R_3: ~4.8×10^3 Ω cm^2) or even relatively high temperatures. This suggests that the light-induced thermal heating of the battery can effectively reduce the impedance of the ASS lithium-air battery, thus enabling the operation of the battery at extra-low temperature.

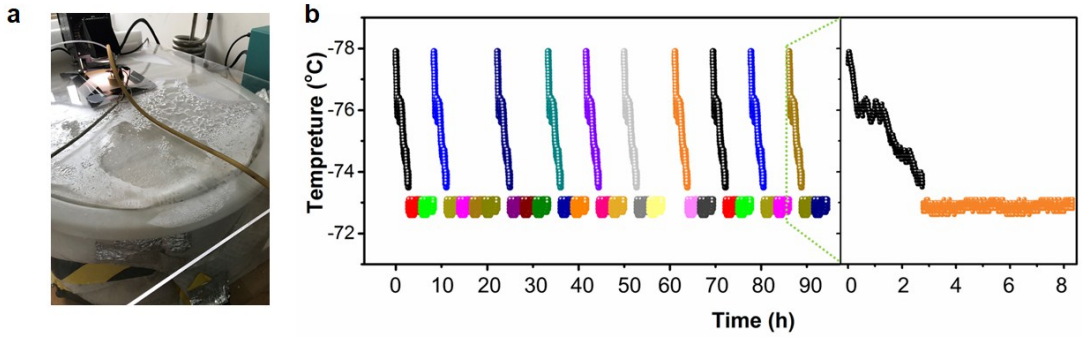

Fig. S8. (a) Optical image of all-solid-state Li-air battery based on plasmonic air cathode operating at low temperature where a low temperature environmental below -73 °C is provided by use of the dry ice (solid-sate CO_2). Xe-lamp was used as light irradiation source. (b) Temperature changes of test system during the discharge/change process where dry ice was added about every eight hours. The temperature around the battery is maintained a stable value (-73 °C) during the discharge/charge cycles.

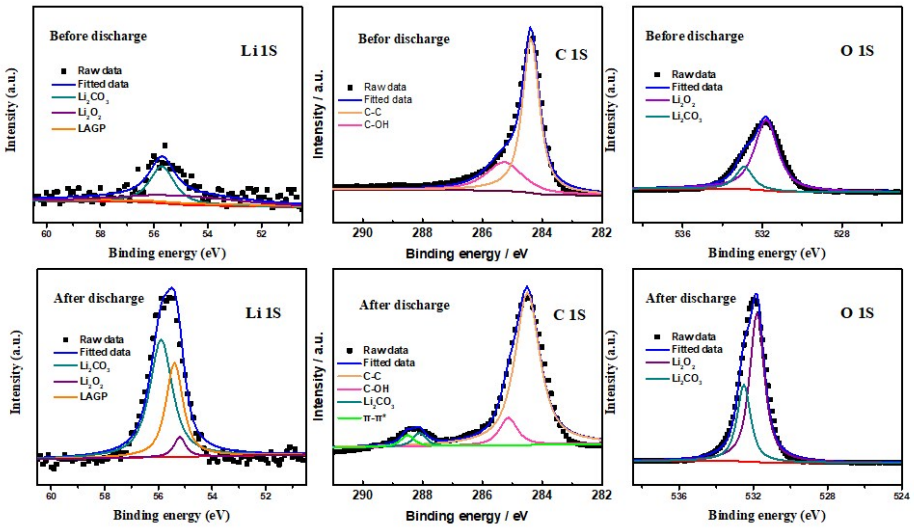

Fig. S9. (a) XPS spectrum of all-solid-sate Li-air batteries before and after discharge.